ACS OMEGA

http://pubs.acs.org/journal/acsodf

Article

Composites of Vanadium (III) Oxide (V_2O_3) Incorporating with Amorphous C as Pt-Free Counter Electrodes for Low-Cost and High-Performance Dye-Sensitized Solar Cells

Kezhong Wu,* Yingshan Wu, Pengyuan Fu, Dandan Yang, Bei Ruan, Mingxing Wu,* and Ruitao Wu*

Cite This: *ACS Omega* 2021, 6, 11183−11191

Read Online

ACCESS | Metrics & More | Article Recommendations | Supporting Information

ABSTRACT: To replace precious Pt-based counter electrodes (CEs) with a low-cost Pt-free catalyst of CEs is still a motivating hotspot to decrease the fabrication cost of dye-sensitized solar cells (DSSCs). Herein, four different V_2O_3@C composite catalysts were synthesized by pyrolysis of a precursor under N_2 flow at 1100 °C and further served as catalytic materials of CEs for the encapsulation of DSSCs. The precursors of V_2O_3@C composites have been prepared via a sol−gel method using different proportions of V_2O_5 with soluble starch in a H_2O_2 solution. Power conversion efficiencies (PCEs) of 3.59, 4.79, 5.15, and 5.06% were obtained from different V_2O_3@C composites, with soluble starch-to-V_2O_5 mass ratios (S/V) of 1:2, 1:1, 2:1, and 4:1, respectively, as CEs to reduce iodide/triiodide in DSSCs. The improvement of electrode performance is due to the combined effects on the increased specific surface area and the enhanced conductivity of V_2O_3@C composite catalysts.

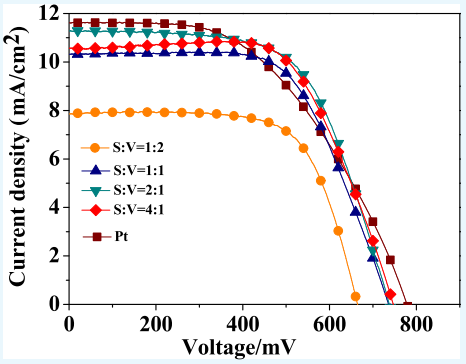

1. INTRODUCTION

Solar energy, a kind of renewable energy source, is rich in reserves, clean, and environmentally friendly. It is rarely limited by the geographical scope. However, it is also easily affected by natural factors such as season, climate, day and night, latitude, altitude, and so on and has intermittent and unstable characteristics. To overcome the above problems, dye-sensitized solar cells (DSSCs) had already been applied to store solar energy through the direct conversion of photo-electricity and to further utilize it.[1,2] The optimization of each of the key parts in a DSSC has been widely mentioned corresponding to the porous semiconductor film photo-anode,[3−5] sensitized dye,[6] electrolytes for redox mediation,[7] and counter electrodes (CEs).[8] Among these components, CEs, as an indispensable part of DSSCs, have two main functions: connecting the external circuit to transmit electrons and catalyzing redox pairs in electrolytes to recycle and regenerate. At present, the focus of research on CEs should be consistent, that is, to maintain high power conversion efficiencies (PCEs) and to further reduce the cost-effectiveness of CEs at the same time by Pt-free electrocatalytic materials to replace the traditional noble Pt-based catalyst of CEs.[9] Herein, the respective research places particular emphasis on the differences in the composition, preparation, morphology, or optimization of the corresponding catalytic materials, and so on. Hence, a variety of Pt-free materials, for instance, carbonaceous materials,[10−14] organic conductive polymers,[15−18] transition-metal compounds (TMCs),[19−24] alloys,[25,26] metal−organic frameworks (MOFs),[27−29] and multi-component compounds,[30−33] have been extended as CE materials to replace the high-cost Pt. These materials as CEs in DSSCs have many advantages of abundance, low cost, easy synthesis, and high stability with large electrochemical activity for the regeneration reactions of I_3^-/I^-.

Among the above catalytic materials of CEs, transition-metal oxides (TMOs) of group VB and VIB, as one of the TMCs, are widely applied to the novel Pt-free CEs due to a similar d-band electron density to that of Pt.[34] In VB group oxides of TMOs, V element of V-based oxides could be diverse in the valence state between V^{2+} and V^{5+}, and it exists in various forms from VO_{2n-1} to VO_{2n+1}. The extensive interest in V-based oxides as catalysts in various electrochemical devices (batteries, supercapacitors, etc.) is because of their unmatched structural types, multiphase states, and easy modification.[35,36] As shown in our previous work,[37] V_2O_3-based CEs had been successfully prepared using $VOCl_3$ as metal precursors with the urea−metal route. The DSSCs using V_2O_3 CEs showed a decent PCE value of 5.40%. Vijayakumar et al. also reported that V_2O_3 nanofiber CEs yielded an efficiency of 5.0%.[38] To further improve the performance and reduce the costs of DSSCs, researchers have focused on producing single V_2O_3 catalysts

Received: December 2, 2020
Accepted: April 8, 2021
Published: April 22, 2021

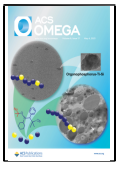

better by incorporating with carbon or carbon-derived materials because of the outstanding conductivity, controllable specific surface, and low-cost fabrication of carbonaceous materials.[39,40] Additional carbonaceous materials as a basic carrier could change the energy band structure and distort the lattice, which result in high-energy activation to improve the electrical conductivity and provide more reaction sites in V-based oxides.[41] Also, in our work, V_2O_3@AC composite catalysts have been fabricated by the pyrolysis of NH_4VO_3 with different mass ratios of activated carbon (AC) at high temperatures.[42] Compared with the 4.54% PCE of Pt and 3.33% of pure V_2O_3, the DSSCs using V_2O_3@AC composite can reach the highest PCE of 5.55% for the regeneration of the I_3^-/I^- redox couple. Gnanasekar et al. wrapped monoclinic crystal VO_2 on one-dimensional carbon as a cost-effective CE and achieved a PCE of 6.53%.[43] As a result, it is significant to explore a stabler, cheaper, and simpler assembly and higher activity to improve the performance of Pt-free CEs in DSSCs.

Herein, different proportions of V_2O_3@C composite catalysts were synthesized via pyrolysis of a precursor under N_2 flow by a solid-state reaction at high temperatures. The precursors were obtained by a sol−gel method with soluble starch (denoted as S) as a carbon source and V_2O_5 (denoted as V) as a metal source in H_2O_2. Soluble starch is a kind of common natural biomass material, which has a large specific surface area and shows flammability and network cross-linking; therefore, it is suitable to be used as a carbon source of composite catalysts.[44−46] The introduction of soluble starch into the precursor can reduce the sintering temperature, accelerate the diffusion rate, and even impel grain growth, which makes it easier to control and optimize the composition and structure of V-based oxides.[47] In this work, four proportions of V_2O_3@C composites with specific composition, structure, morphology, and properties were obtained by guided pyrolysis from different mass ratios (S/V) of 1:2, 1:1, 2:1, and 4:1. The structural characterization of V_2O_3@C composites (S/V) was investigated by X-ray diffraction (XRD), scanning electron microscopy (SEM), and N_2 adsorption/desorption analysis, and the corresponding electrochemical performance and basic parameters were determined by different electrochemical testing techniques.

2. RESULTS AND DISCUSSION

2.1. Material Characterization. Figure 1 presents the details of diffraction angles of four V_2O_3@C (S/V) and the pure V_2O_3 at 32.9, 36.2, 37.8, 41.1, 43.6, 49.8, 54.0, 58.2, 63.6, 65.1, 71.0, 76.2, 78.3, 80.5, 82.0, and 86.21°, which can be indexed to the crystal facets of the pristine V_2O_3 in (104), (110), (006), (113), (202), (024), (116), (122), (214), (300), (101), (220), (306), (223), (312), and (134), respectively. The XRD peaks of V_2O_3@C (S/V = 1:2, 1:1) were similar to those of pure V_2O_3. With the increase in the proportion of soluble starch in the precursor, the prepared V_2O_3@C (S/V = 2:1, 4:1) showed an additional wide and weak pattern at around 24.9°, which is caused by the (002) facet diffraction of amorphous C,[48,49] and further demonstrated noncrystalline C incorporating with V_2O_3 as a carrier by soluble starch carbonized at high temperatures without affecting the diffraction patterns of V_2O_3. The strong diffraction patterns of V_2O_3 in the composites almost cover the broad and low diffraction patterns of amorphous C due to the highly ordered crystal structure of V_2O_3 in the composites.

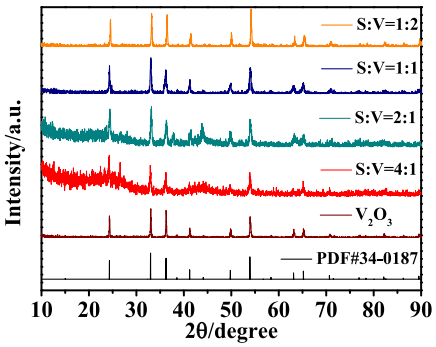

Figure 1. XRD patterns of the four prepared V_2O_3@C composites (S/V) and pure V_2O_3.

The morphologies of four V_2O_3@C (S/V) and the as-prepared pure V_2O_3 were observed in Figure 2. The special characterization of pure V_2O_3 particles belongs to a solid block material with compact apparent density and less pores in Figure 2e. The shape of pure V_2O_3 was an irregular sphere with particle size in the range of 100−550 nm. The nanostructures of V_2O_3@C (1:2 and 1:1) all presented that the particle shapes were sphere, potato, ellipsoids, etc., with the particle size distribution in a relatively narrow range of 50−150 nm. Also, SEM results show that there is no excess amorphous C on the surface of V_2O_3@C (1:2, 1:1), as in Figure 2a,b, indicating that the soluble starch almost completely reacts with V_2O_5 to form V_2O_3 in the precursor. With further increase in the soluble starch mass ratio, V_2O_3@C (2:1, 4:1) obviously composed of two different components, including V_2O_3 and amorphous C, as observed from Figure 2c,d. The smaller flocculate C fills the gaps among V_2O_3 particles with uniform distribution in the analysis of SEM, that is, embodiment of amorphous substances. In particular, the V_2O_3 morphologies in V_2O_3@C (2:1) show low apparent density and open structure as nanoscale jars with a diameter of 50−100 nm and a wall thickness of about 15 nm, as shown in Figure 2c. The surface of V_2O_3@C (2:1) has several uniformly distributed open nanojars that would improve the effective surface area of the material particles, increase the number of catalytic sites, and greatly promote the electrocatalytic performance of CEs.[41] Simultaneously, there is moderate dual connectivity that consists of uninterrupted nanoparticles and interconnected pore channels in V_2O_3@C (2:1), which should be an alternative Pt material with high effective catalytic activity as CEs.[50,51] However, the excess carbonization of soluble starch in V_2O_3@C (4:1) results in that most of the surface of V_2O_3 was covered by smaller flocculate C particles (Figure 2d). The higher the amount of soluble starch, the smaller the V_2O_3 particle size, and the particle morphology becomes more and more spherical, which shows the isotropic growth with a narrower average particle size of <10 nm. This determination of morphology coincides with amorphous carbon in the V_2O_3@C composites by X-ray diffraction results. Energy-dispersive X-ray (EDX) analysis was further carried out to confirm the elements V, O, and C within V_2O_3@C (2:1), as in Figure 2f. EDX patterns of other CE composite materials showed similar results, but only the content of the elements was different.

The N_2 adsorption−desorption isotherms of V_2O_3@C (S/V) all exhibited narrow loops complying with a type-IV isotherm that indicate that four V_2O_3@C materials are mesoporous, and the pure V_2O_3 can be identified by an

https://doi.org/10.1021/acsomega.0c05880
ACS Omega 2021, 6, 11183−11191

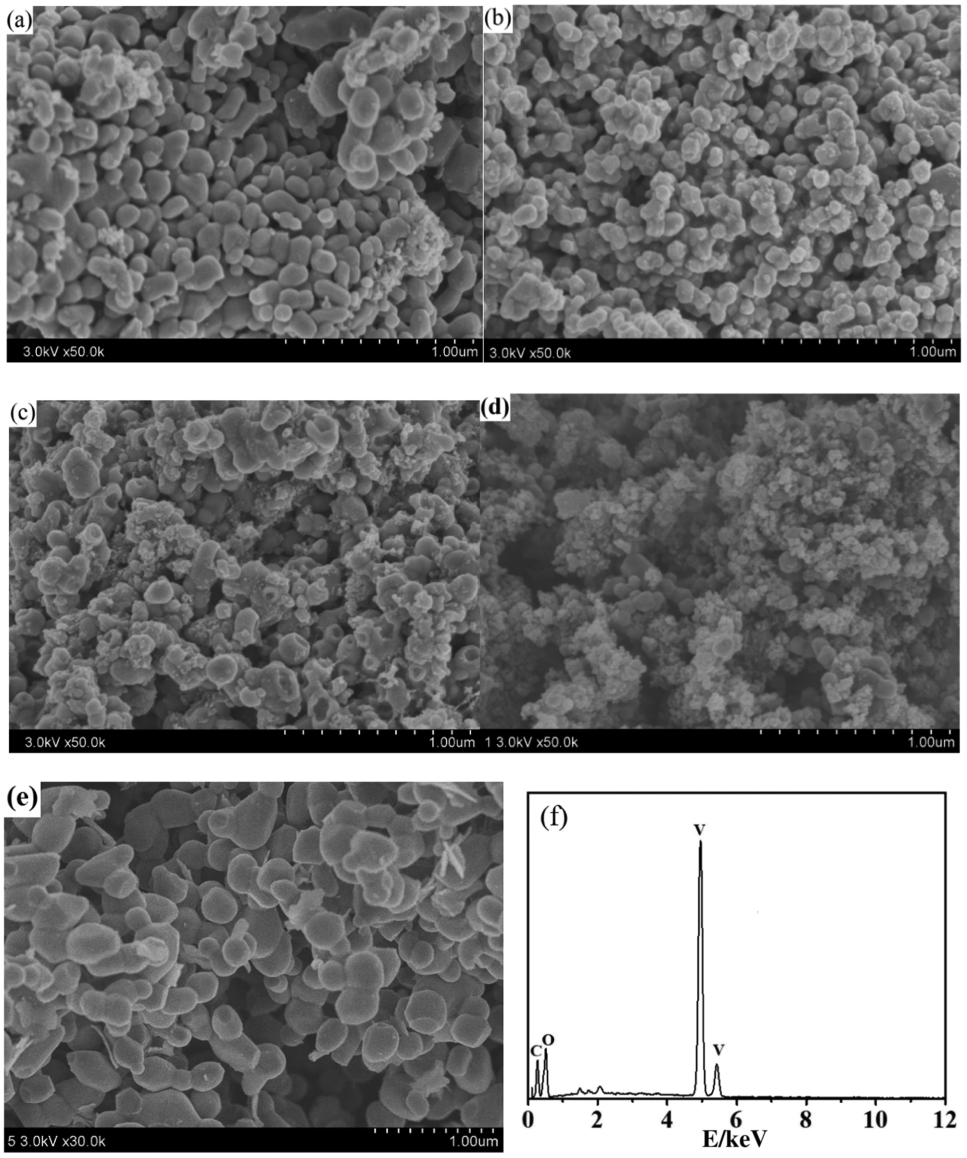

Figure 2. (a–d) SEM images of V_2O_3@C with S/V = 1:2, 1:1, 2:1, 4:1 and (e) pure V_2O_3. (f) EDX pattern (2:1).

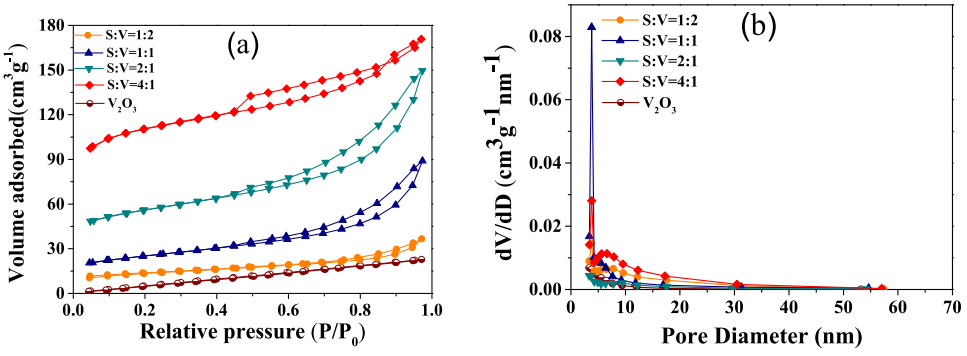

Figure 3. (a) N_2 adsorption–desorption isotherms and (b) d_p of V_2O_3@C (S/V) and pure V_2O_3.

unapparent hysteresis loop belonging to a type-I characteristic of isotherms, as shown in Figure 3.[52] With the increase in the soluble starch mass ratio, the hysteresis loop integral areas of V_2O_3@C composites gradually increase. Table 1 shows that the S_{BET} values of S/V = 4:1 (350.2 m^2/g) and 2:1 (181.7 m^2/g) are higher than those of 1:1 (85.1 m^2/g), 1:2 (45.5 m^2/g), and V_2O_3 (33.5 m^2/g); the V_p values follow an increasing order: 0.171 (2:1) > 0.116 (4:1) > 0.115 (1:1) > 0.040 (1:2) > 0.031 cm^3/g (V_2O_3); the d_p values of 3.368, 3.782, 3.798, 3.795, and 3.361 nm were obtained from S/V = 1:2, 1:1, 2:1, 4:1, and pure V_2O_3, respectively. These data indicate that the pure V_2O_3 was a solid bulk material with a lower V_p and a very

https://doi.org/10.1021/acsomega.0c05880
ACS Omega 2021, 6, 11183–11191

Table 1. Textural Properties of V_2O_3@C (S/V) and Pure V_2O_3

materials	S_{BET} (m^2/g)	V_p (cm^3/g)	d_p (nm)
S/V = 1:2	45.5	0.040	3.368
S/V = 1:1	85.1	0.115	3.782
S/V = 2:1	181.7	0.171	3.798
S/V = 4:1	350.2	0.116	3.795
V_2O_3	33.5	0.031	3.361

small S_{BET}, and the amorphous C incorporated with V_2O_3 could offer a larger V_p value for I_3^-/I^- diffusion and more active edge sites for the regeneration of I_3^-/I^-.[53] Because too much amorphous C covers the surface of the material, V_p and d_p of V_2O_3@C (4:1) were smaller than those of V_2O_3@C (2:1). The porous structure of four V_2O_3@C composites is (S/V) also in good agreement with the SEM (Figure 2) results.

2.2. Electrochemical Properties of Electrodes. The redox reaction of $I_3^- + 2e^- \rightarrow 3I^-$ occurs on the interface between CEs and the electrolyte to recycle and regenerate the I_3^-/I^- pairs of DSSCs at a low potential.[54] Two key parameters ΔE_p (peak-to-peak separation) and I_P (current density of cathodic peak) can be determined from the CV profile to evaluate the electrocatalytic activity of the electrode. Figure 4

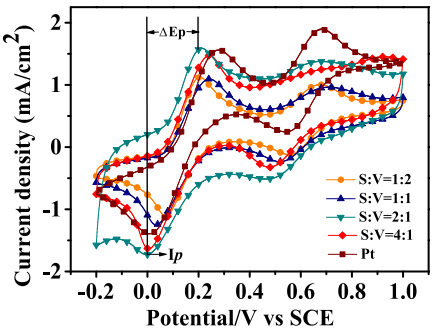

Figure 4. CV profile of V_2O_3@C (S/V) and Pt CEs.

shows ΔE_p values of 0.150 (1:2), 0.205 (1:1), 0.202 (2:1), and 0.229V (4:1) and I_P values of 1.092 (1:2), 1.238 (1:1), 1.724 (2:1), and 1.636 (4:1) in V_2O_3@C (S/V) CEs. The smaller the ΔE_p value, the larger the electrocatalytic ability and reversibility of the I_3^-/I^- regeneration reactions, which would be beneficial to the enhancement of DSSC performance.[41] In theory, $\Delta E_p \propto 1/k_s$, where k_s is the rate constant of electrochemical reaction.[55] Thus, smaller ΔE_p values indicate that the reaction of $I_3^- + 2e^- \rightarrow 3I^-$ can be carried out at a rapid rate on CEs.[56] The larger I_P can also demonstrate the catalytic material on CEs to more effectively catalyze the reduction of I_3^- to I^-. Comparing the ΔE_p and I_P values of four kinds of V_2O_3@C (S/V) with Pt, the corresponding values of V_2O_3@C (2:1 and 4:1) are better than those of Pt CEs (0.151 V, 0.534 mA/cm^2). Therein, in the V_2O_3@C composite (2:1), the open nanojar V_2O_3 incorporated with amorphous C and activated by high temperature and N-doping provided suitable dual connectivity and more vacancies and defects, which result in lower ΔE_p and higher I_P values.[57,58] The V_2O_3@C composite (2:1) as a Pt-free efficient CE would be favorable to enhance the electrocatalytic activity in DSSCs. For the expected catalyst, it is important to evaluate the long-term stability of the catalytic property. Herein, the V_2O_3@C (2:1) material as a CE catalyst was assessed by 30 consecutive CV cycles. There are minor I_P attenuation and little redox peak position shift of $I_3^- + 2e^- \rightarrow 3I^-$, which demonstrate that V_2O_3@C CEs possess stability as well as increased catalytic activity against I_3^-/I^- redox couples.

The characteristic electrochemical impedance spectroscopy (EIS) parameter values of R_{ct} (charge transfer resistance), R_s (solution resistance), and Z_w (Warburg impedance) were collected from the Nyquist plots of the symmetric cells with different V_2O_3@C (S/V) and Pt CEs in Figure 5. The

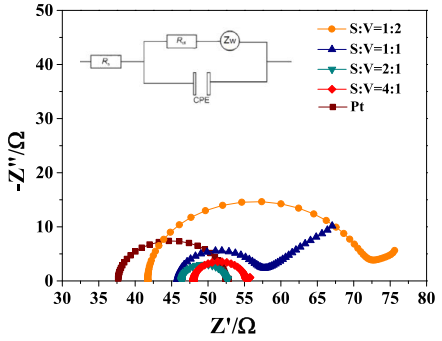

Figure 5. Nyquist plots of V_2O_3@C (S/V) and Pt CEs for symmetrical cells.

increasing order of values of R_{ct} is 28.81 Ω (1:2) > 14.8 Ω (Pt) > 10.72 Ω (1:1) > 7.10 Ω (4:1) > 6.08 Ω (2:1). R_s values of 41.71, 45.82, 46.38, 48.01, and 37.66 Ω and Z_w values of 0.064, 0.050, 0.114, 0.103, and 0.126 Ω were obtained from S/V = 1:2, 1:1, 2:1, 4:1, and Pt CEs, respectively. The R_{ct} values of V_2O_3@C (4:1, 2:1) are much smaller than those of other V_2O_3@C (S/V) and Pt. In the preparation process of CE composite catalyst materials, the carbonization of soluble starch with cross-linking and natural adhesion can result in the improvement of the dispersion uniformity of flocculate amorphous C in the precursor. Hence, V_2O_3 incorporating with amorphous C can very meaningfully provide that the continuous conductive layers in between the interface of V_2O_3@C composites transfer electrons and the interconnective pore channels permeate and diffuse I_3^-/I^- electric pairs in the electrolyte.[50,59] Furthermore, the Warburg impedance (Z_w) of V_2O_3@C (S/V) shows a similar 45° straight line, indicating that the reaction of $I_3^- + 2e^- \rightarrow 3I^-$ indicates the charge transfer process rather than the mass transport process.

The exchange current density (J_0) of Tafel polarization was determined as four different V_2O_3@C (S/V) and Pt CEs in the reduction of $I_3^- + 2e^- \rightarrow 3I^-$, as shown in Figure 6. A larger J_0

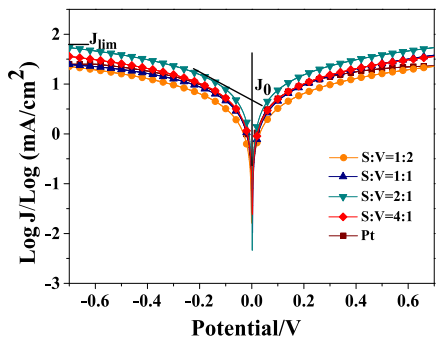

Figure 6. Tafel curves of V_2O_3@C (S/V) and Pt CEs based on symmetrical cells.

https://doi.org/10.1021/acsomega.0c05880
ACS Omega 2021, 6, 11183−11191

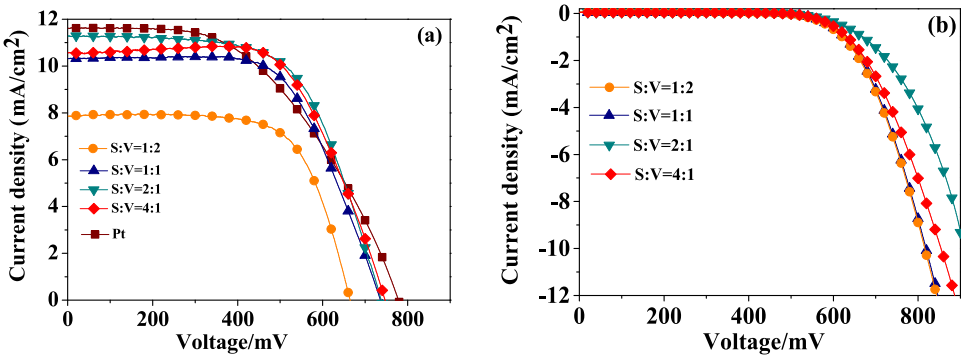

Figure 7. $J-V$ characteristics of DSSC assembled with various CEs: (a) I = 100 mW/cm^2 and (b) in the dark.

value means that a small applied potential results in an appreciable increase in current.[60] Tafel polarization results show J_0 values of four different V_2O_3@C and Pt CEs in the following order: 2:1 (0.669 mA/cm^2) > 4:1 (0.529 mA/cm^2) > Pt (0.501 mA/cm^2) > 1:1 (0.482 mA/cm^2) > 1:2 (0.294 mA/cm^2). Particularly, V_2O_3@C (2:1) CEs show the largest slope of extrapolated straight lines in the Tafel zone of anodic and cathodic branches, which revealed the largest J_0 compared to other V_2O_3@C (S/V) and Pt CEs. The Tafel polarization results indicate that V_2O_3@C composites (2:1, 4:1) possess a lower polarization potential and a quicker charge exchange rate on the interface between I_3^- and V_2O_3@C than that of Pt CEs in DSSCs. In conclusion, the excellent performance of V_2O_3@C composite (2:1) CEs can be attributed to the moderate dual connectivity with continuous nanoparticles and interconnected pore channels compared to other CEs.

2.3. Application of V_2O_3@C Composites in DSSCs. To make a direct comparison of performance with different V_2O_3@C (S/V) and Pt as CEs in encapsulated DSSCs, the $J-V$ (photocurrent−photovoltage) curves were characterized under I = 100 mW/cm^2 of a solar simulator (Figure 7). Four different V_2O_3@C CEs presented V_{oc} (open-circuit voltage) values of 665, 736, 738, and 747 mV, J_{sc} (short-circuit current density) values of 7.88, 10.31, 11.31, and 10.56 mA/cm^2, fill factor (FF) values of 0.62, 0.63, 0.62, and 0.64, and PCE values of 3.59, 4.79, 5.15, and 5.06%, which were, respectively, obtained from S/V = 1:2, 1:1, 2:1, and 4:1, as shown in Table 2. Because of the same dye-sensitized

Table 2. Performances of DSSCs Assembled with V_2O_3@C (S/V) and Pt CEs

CEs	V_{oc} (mV)	J_{sc} (mA/cm^2)	FF	PCE (%)
S/V = 1:2	665	7.88	0.62	3.59
S/V = 1:1	736	10.31	0.63	4.79
S/V = 2:1	738	11.31	0.62	5.15
S/V = 4:1	747	10.56	0.64	5.06
Pt	779	11.63	0.50	4.54

commercial TiO_2 photoanode used in the process of assembling DSSC devices, the performances of DSSCs only depend on the electrocatalytic reduction of redox couples at CEs, and different CEs also affect the photocurrent generation at the photoanode through dye regeneration. Comparing the parameters (J_{sc}, FF, V_{oc}, PCE) of four V_2O_3@C (S/V) under the encapsulation of DSSC in the same way, the J_{sc} value of V_2O_3@C (2:1) is the largest and the four FF values are close to 0.63 ± 0.01. The enhanced J_{sc} value of V_2O_3@C (2:1) can be attributed to its open nanoscale jar morphology with the larger number of catalytic activity sites, continuity channel, and low R_{ct}.[61] V_{oc} is the difference between the Fermi level of the semiconducting material and the potential energy level of the redox potential in the liquid electrolyte.[62] It should be noted that the V_{oc} values of V_2O_3@C (S/V) have a little enhancement with the increase in amorphous C. The variation of V_{oc} in the different CEs for DSSCs can be influenced by the surface area of CEs. Despite the exposed geometric area of all V_2O_3@C composite CEs being 0.5 cm × 0.5 cm, the actual electrochemical active area is different due to the existence of amorphous C in different proportions. The highest value of V_{oc} for V_2O_3@C composite (4:1) CE may be attributed to its much rougher surface with the maximum S_{BET} compared to other CEs.[63] FF is the ratio of the maximum power of DSSCs to the product of V_{oc} and J_{sc}. In the $J-V$ curve of DSSCs, the more rectangular the output characteristics representing the level of PCE, the higher the FF. The FF value is closely related to the concentration gradients in DSSCs.[64] It can be seen that the PCEs of V_2O_3@C (1:1, 2:1, and 4:1) CEs are higher than 4.54% of Pt CEs (J_{sc} = 11.63 mA/cm^2, V_{oc} = 779 mV, and FF = 0.50). Although V_2O_3@C (2:1) CE has a lower V_{oc} than V_2O_3@C (4:1), its overall efficiency is higher than that of V_2O_3@C (4:1) due to various combined factors. Therein, V_2O_3@C (2:1) CEs yielded the highest PCE (5.15%) in DSSCs. The remarkably enhanced J_{sc} value had a great contribution to the highest PCE of V_2O_3@C (2:1) as CEs. With the change of mass ratio (S/V) from 1:2 to 2:1, the PCE of the V_2O_3@C composites (S/V) gradually increases. However, on further increasing the S/V from 2:1 to 4:1, the PCE of V_2O_3@C (4:1) was lower than that of V_2O_3@C (2:1). The possible reason is that too much amorphous C in the V_2O_3@C (4:1) could lead to the decrease of the electron transfer rate in the puffy materials, and the O_x in the electrolyte could show a dark current between the photogenerated electrons and dye holes as well as V_2O_3@C (4:1) CEs with lower J_{sc} values.[65] The dark $J-V$ curves revealed that DSSCs using V_2O_3@C (2:1) CEs present much lower dark current than those of DSSCs using other CEs, as in Figure 7b. That is to say, different degrees of current leakage occurred in DSSCs using V_2O_3@C composites. This result not only alludes to the suppression of the electron recombination at the CEs/electrolyte interface but also agrees well with the enhanced J_{sc} values of DSSCs. The $J-V$ experimental results confirmed that the improved PCE and J_{sc} performances should be mainly attributed to the excellent electrocatalytic activity of V_2O_3@C composite catalysts by V_2O_3 incorporating an appropriate amount of amorphous C.

https://doi.org/10.1021/acsomega.0c05880
ACS Omega 2021, 6, 11183−11191

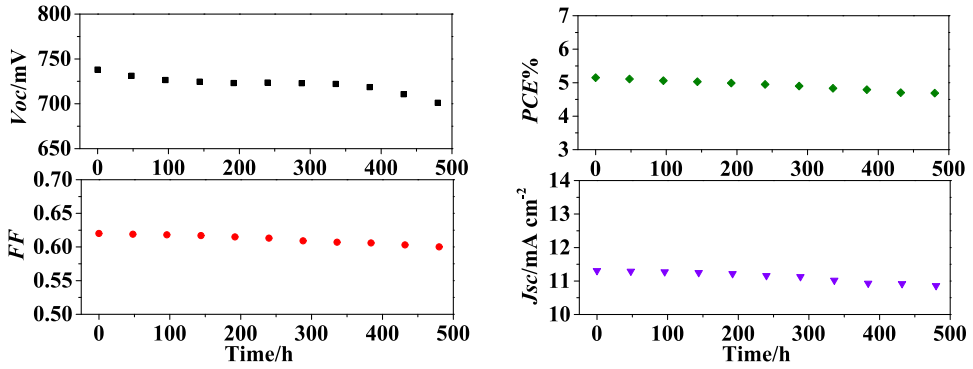

Figure 8. Stability of V_2O_3@C composites (2:1) as CEs in DSSCs.

According to the above-mentioned characterization results of CV, EIS, Tafel, and *J*−*V*, V_2O_3@C composite CEs as Pt-free catalysts can highly and effectively catalyze the reduction of $I_3^- + 2e^- \rightarrow 3I^-$ and further improve the PCE of DSSCs. In addition, it is very important that DSSCs should keep long stability along with maintaining high PCEs as competitive energy storage systems. As shown in Figure 8, a long-term stability test of the DSSCs using V_2O_3@C (2:1) CEs was performed after 500 h, and the photovoltaic parameters of V_{oc}, J_{sc}, FF, and PCE retained 95, 96, 97, and 91% of their initial values, respectively. The high stability of DSSCs can be attributed to the fact that V_2O_3 incorporating with amorphous C possesses higher electrical conductivity and highest mechanical stability. The excellent stability of V_2O_3@C composite CEs as their intrinsic features makes them more suitable as Pt-free materials for low-cost and long-term-stable DSSCs.

3. CONCLUSIONS

In various syntheses of V-based oxides, the choice of reactants and reaction process will directly affect the difference in the material properties. Thus, in this work, eco-friendly soluble starch was carbonized to amorphous C at high temperatures; the amorphous C incorporating with V_2O_3 to prepare V_2O_3@C composites can cause various volume defects, enhance the surface energy and adsorption, shorten the time of electron and hole migration to the particle surface, and improve the conductivity and catalysis. The DSSCs using V_2O_3@C composite (S/V) CEs with S/V = 1:1, 2:1, and 4:1, respectively, obtained PCEs of 4.79, 5.15, and 5.06% from *J*−*V* measurements, which were higher than the PCEs of 4.54% and 3.33% for Pt and pure V_2O_3 CEs, respectively, for the regeneration of I_3^-/I^- redox couple. The corresponding electrochemical performance and basic parameters were determined by CV, EIS, Tafel, and *J*−*V* characterizations revealing that V_2O_3@C composite (S/V) CEs can catalyze the regeneration of I_3^-/I^- higher than Pt CEs. Pt-free CEs are expected to be highly efficient and stable in the practical application of DSSCs as well as to expand the range of CE catalyst selection in the future.

4. EXPERIMENTAL SECTION

4.1. Materials. Vanadium pentoxide (V_2O_5, purity >99%) and hydrogen peroxide (H_2O_2, 10 wt %) were purchased from Shanghai Reagent Factory. The soluble starch and ammonium vanadate (NH_4VO_3, purity >99%) were purchased from Aladdin, Shanghai. All chemicals are of analytical reagent (AR) grade and used as received without purification. Deionized water was obtained from an electrothermal distiller and was used in all experiments.

4.2. Synthesis of V_2O_3@C Composites. V_2O_3 was directly prepared by the pyrolysis of NH_4VO_3 under high-purity N_2 flow (50 sccm) at 1100 °C for 1 h. The precursor of V_2O_3@C composites (S/V) was prepared via a sol−gel method. First, 0.4 g of V_2O_5 was slowly dissolved in 30 mL of 10 wt % H_2O_2 solution and stirred evenly. With the violent reaction in the solution, a large number of bubbles emerge. After standing for 10 h, 0.2, 0.4, 0.8, and 1.6 g of the soluble starch were, respectively, added into the homogeneous mixed solution with vigorous stirring. The same four solutions were heated from ambient temperature to 80 °C until the soluble starch in each solution was completely dissolved. All of the four solutions gradually became a red flocculent sol with the volatilization of the solvent and finally turned into a dark green gel. After drying in a vacuum oven at 50 °C for 4 h, the as-precursor was milled for 0.5 h and further formed an 11.5 mm diameter and 10 mm thick tablet by a hydraulic tablet-press at 4 MPa. Then, the four proportions of V_2O_3@C composite (S/V) catalysts were synthesized via pyrolysis of the precursor under N_2 flow (50 sccm) at 1100 °C for 1 h.

4.3. Assembly of DSSCs. The assembly of DSSCs is shown in the Supporting Information.

4.4. Characterization and Electrochemical Measurements. The characterization and electrochemical measurements of CEs are shown in the Supporting Information.

■ ASSOCIATED CONTENT

Supporting Information

The Supporting Information is available free of charge at https://pubs.acs.org/doi/10.1021/acsomega.0c05880.

Assembly of dye-sensitized solar cells (DSSCs) and characterization and electrochemical measurements of counter electrodes (CEs) (PDF)

■ AUTHOR INFORMATION

Corresponding Authors

Kezhong Wu − *Hebei Key Laboratory of Inorganic Nanomaterials, College of Chemistry and Materials Science, Hebei Normal University, Shijiazhuang 050024, China;* orcid.org/0000-0002-7987-4637; Email: kzwu@hebtu.edu.cn

Mingxing Wu − *Hebei Key Laboratory of Inorganic Nanomaterials, College of Chemistry and Materials Science, Hebei Normal University, Shijiazhuang 050024, China;* Email: mingxing.wu@hebtu.edu.cn

https://doi.org/10.1021/acsomega.0c05880
ACS Omega 2021, 6, 11183−11191

Ruitao Wu − *Hebei Key Laboratory of Inorganic Nanomaterials, College of Chemistry and Materials Science, Hebei Normal University, Shijiazhuang 050024, China*; Email: wuruitao@vip.sina.com

Authors

Yingshan Wu − *Hebei Key Laboratory of Inorganic Nanomaterials, College of Chemistry and Materials Science, Hebei Normal University, Shijiazhuang 050024, China*

Pengyuan Fu − *Hebei Key Laboratory of Inorganic Nanomaterials, College of Chemistry and Materials Science, Hebei Normal University, Shijiazhuang 050024, China*

Dandan Yang − *Hebei Key Laboratory of Inorganic Nanomaterials, College of Chemistry and Materials Science, Hebei Normal University, Shijiazhuang 050024, China*

Bei Ruan − *Hebei Key Laboratory of Inorganic Nanomaterials, College of Chemistry and Materials Science, Hebei Normal University, Shijiazhuang 050024, China*

Complete contact information is available at: https://pubs.acs.org/10.1021/acsomega.0c05880

Notes

The authors declare no competing financial interest.

■ ACKNOWLEDGMENTS

This work was financially supported by the National Natural Science Foundation of China (21973026), the Natural Science Foundation of Hebei Province (B2019205249), and the Science Foundation of Hebei Normal University (L2019Z02).

■ REFERENCES

(1) O'Regan, B.; Grätzel, M. A low-cost, high-efficiency solar-cell based on dye-sensitized colloidal TiO_2 films. *Nature* **1991**, *353*, 737−740.

(2) Chen, M.; Shao, L.-L.; Qian, X.; Ren, T.-Z.; Yuan, Z.-Y. Direct synthesis of cobalt nanoparticle-imbedded mesoporous carbons for high-performance dye-sensitized solar cell counter electrodes. *J. Mater. Chem. C* **2014**, *2*, 10312−10321.

(3) Akın, S.; Açıkgoz, S.; Gulen, M.; Akyurek, C.; Sonmezoglu, S. Investigation of the photoinduced electron injection processes for natural dye-sensitized solar cells: the impact of anchoring groups. *RSC Adv.* **2016**, *6*, 85125−85134.

(4) Sönmezoğlu, Ö. A.; Akın, S.; Terzi, B.; Mutlu, S.; Sonmezoglu, S. An effective approach for high-efficiency photoelectrochemical solar cells by using bifunctional DNA molecules modified photoanode. *Adv. Funct. Mater.* **2016**, *26*, 8776−8783.

(5) Akın, S.; Ulusu, Y.; Waller, H.; Lakey, J. H.; Sonmezoglu, S. Insight into interface engineering at TiO_2/dye through molecularly functionalized Caf1 biopolymer. *ACS Sustainable Chem. Eng.* **2018**, *6*, 1825−1836.

(6) Chebrolu, V.; Kim, H. Recent progress in quantum dot sensitized solar cells: an inclusive review of photoanode, sensitizer, electrolyte, and the counter electrode. *J. Mater. Chem. C* **2019**, *7*, 4911−4933.

(7) Wu, M.-X.; Lin, Y.-N.; Guo, H.-Y.; Li, W.-Y.; Wang, Y.-D.; Lin, X. Design a novel kind of open-ended carbon sphere for a highly effective CE catalyst in dye-sensitized solar cells. *Nano Energy* **2015**, *11*, 540−549.

(8) Wu, J.-H.; Lan, Z.; Lin, J.-M.; Huang, M.-L.; Huang, Y.-F.; Fan, L.-Q.; Luo, G.-G.; Lin, Y.; Xie, Y.-M.; Wei, Y.-L. Counter electrodes in dye-sensitized solar cells. *Chem. Soc. Rev.* **2017**, *46*, 5975−6023.

(9) Wu, M.-X.; Ma, T.-L. Recent progress of counter electrode catalysts in dye-sensitized solar cells. *J. Phys. Chem. C* **2014**, *118*, 16727−16742.

(10) Jing, H.-Y.; Shi, Y.-T.; Qiu, W.-W.; Wu, D.-D.; Song, X.-D.; An, Y.-L.; Hao, C. Onion-like graphitic carbon covering metallic nanocrystals derived from brown coal as a stable and efficient counter electrode for dye-sensitized solar cells. *J. Power Sources* **2019**, *414*, 495−501.

(11) Rakspun, J.; Chiang, Y.; Chen, J.; Yeh, C.; Amornkitbamrung, V.; Chanlek, N.; Vailikhit, V.; Hasin, P. Modification of reduced graphene oxide layers by electron-withdrawing/donating units on molecular dopants: Facile metal-free counter electrode electrocatalysts for dye-sensitized solar cells. *Sol. Energy* **2020**, *203*, 175−186.

(12) Jayaweera, E.; Kumara, G.; Pitawala, H.; Rajapakse, R.; Gunawardhana, N.; Bandara, H.; Senarathne, A.; Ranasinghe, C.; Huang, H.-H.; Yoshimura, M. Vein graphite-based counter electrodes for dye-sensitized solar cells. *J. Photochem. Photobiol., A* **2017**, *344*, 78−83.

(13) Monreal-Bernal, A.; Vilatela, J.; Costa, R. CNT fibres as dual counter-electrode/current-collector in highly efficient and stable dye-sensitized solar cells. *Carbon* **2019**, *141*, 488−496.

(14) Madhu, R.; Veeramani, V.; Chen, S.-M.; Palanisamy, J.; Ezhil, V. Pumpkin stem-derived activated carbons as counter electrodes for dye-sensitized solar cells. *RSC Adv.* **2014**, *4*, 63917−63921.

(15) Taş, R.; Gulen, M.; Can, M.; Sonmezoglu, S. Effects of solvent and copper-doping on polyaniline conducting polymer and its application as a counter electrode for efficient and cost-effective dye-sensitized solar cells. *Synth. Met.* **2016**, *212*, 75−83.

(16) Zhang, R.; Xu, J.; Qian, J.-N.; Xia, J.-B. Facile synthesis of poly(3,4-ethylenedioxythiophene) and poly(bis-3,4-ethylenedioxythiophene) via UV-irradiation polymerization and their reduction/iodine oxidation post-treatment for the application as counter electrodes for dye-sensitized solar cells. *Electrochim. Acta* **2019**, *313*, 505−512.

(17) Tsai, C.; Huang, W.-C.; Hsu, Y.; Shih, C.; Teng, I.-J.; Yu, Y.-H. Poly(o-methoxyaniline) doped with an organic acid as cost-efficient counter electrodes for dye-sensitized solar cells. *Electrochim. Acta* **2016**, *213*, 791−801.

(18) Taş, R.; Can, M.; Sonmezoglu, S. Exploring on photovoltaic performance of dye-sensitized solar cells using polyaniline as a counter electrode: role of aluminum-aolvent interactions. *IEEE J. Photovoltaics* **2017**, *7*, 792−800.

(19) Gao, C.-J.; Han, Q.-J.; Wu, M.-X. Review on transition metal compounds based counter electrode for dye-sensitized solar cells. *J. Energy Chem.* **2018**, *27*, 703−712.

(20) Xu, T.-T.; Kong, D.-C.; Tang, H.-J.; Qin, X.-L.; Li, X.-H.; Gurung, A.; Kou, K.-C.; Chen, L.-X.; Qiao, Q.-Q.; Huang, W. Transparent MoS_2/PEDOT composite counter electrodes for bifacial dye-sensitized solar cells. *ACS Omega* **2020**, *5*, 8687−8696.

(21) Alkuam, E.; Badradeen, E.; Guisbiers, G. Influence of CdS morphology on the efficiency of dye-sensitized solar cells. *ACS Omega* **2018**, *3*, 13433−13441.

(22) Zhou, R.; Xu, J.; Huang, F.; Ji, F.; Wan, L.; Niu, H.; Mao, X.; Xu, J.; Cao, G. A novel anion-exchange strategy for constructing high performance PbS quantum dot-sensitized solar cells. *Nano Energy* **2016**, *30*, 559−569.

(23) Özel, F.; Sarilmaz, A.; Istanbullu, B.; Aljabour, A.; Kus, M.; Sonmezoglu, S. Penternary chalcogenides nanocrystals as catalytic materials for efficient counter electrodes in dye-synthesized solar cells. *Sci. Rep.* **2016**, *6*, No. 29207.

(24) Akman, E.; Altintas, Y.; Gulen, M.; Yilmaz, M.; Mutlugun, E.; Sonmezoglu, S. Improving performance and stability in quantum dot-sensitized solar cell through single layer graphene/Cu_2S nanocomposite counter electrode. *Renewable Energy* **2020**, *145*, 2192−2200.

(25) Tang, Q.; Zhang, H.; Meng, Y.; He, B.; Yu, L. Dissolution engineering of platinum alloy counter electrodes in dye-sensitized solar cells. *Angew. Chem., Int. Ed.* **2015**, *54*, 11448−11452.

(26) Chen, X.; Tang, Q.; He, B.; Lin, L.; Yu, L. Platinum-free binary Co-Ni alloy counter electrodes for efficient dye-sensitized solar cells. *Angew Chem., Int. Ed.* **2014**, *53*, 10799−10803.

(27) Chen, T.-Y.; Huang, Y.-J.; Li, C.-T.; Kung, C.-W.; et al. Metal-organic framework/sulfonated polythiophene on carbon cloth as a

flexible counter electrode for dye-sensitized solar cells. *Nano Energy* **2017**, *32*, 19−27.
(28) Khajavian, R.; Mirzaei, M.; Alizadeh, H. Current status and future prospects of metal−organic frameworks at the interface of dye-sensitized solar cells. *Dalton Trans.* **2020**, *49*, 13936−13947.
(29) Wang, T.; Li, Y.-J.; Li, H.-S.; Shi, D.-X.; Jiao, Q.-Z.; Zhao, Y.; Su, P.-J.; Wang, W.; Wu, Q. Rational design of hierarchical structural CoSe@NPC/CoSe@CNT nanocomposites derived from metal−organic frameworks as a robust Pt-free electrocatalyst for dye-sensitized solar cells. *ACS Omega* **2020**, *5*, 26253−26261.
(30) Zhu, J.; Tang, M.; He, B.; Zhang, W.; Li, X.; Gong, Z.; Chen, H.; Duan, Y.; Tang, Q. Improved charge extraction through interface engineering for 10.12% efficiency and stable $CsPbBr_3$ perovskite solar cells. *J. Mater. Chem. A* **2020**, *8*, 20987−20997.
(31) Zhou, R.; Yang, Z.; Xu, J.; Cao, G. Synergistic combination of semiconductor quantum dots and organic-inorganic halide perovskites for hybrid solar cells. *Coord. Chem. Rev.* **2018**, *374*, 279−313.
(32) Gulen, M.; Sarilmaz, A.; Patir, I.; Ozel, F.; Sonmezoglu, S. Ternary copper-tungsten- disulfide nanocube inks as catalyst for highly efficient dye-sensitized solar cells. *Electrochim. Acta* **2018**, *269*, 119−127.
(33) Zhang, Y.-N.; Wang, P.-F.; Zhang, T.-Y.; Gou, B.-W. High-efficiency dye-sensitized solar cells based on kesterite $Cu_2ZnSnSe_4$ inlaid on a flexible carbon fabric composite counter electrode. *ACS Omega* **2020**, *5*, 24898−24905.
(34) Zhao, Y.-F.; Wang, S.-J.; Liu, H.; Guo, X.; Zeng, X.-R.; Wu, W.-J.; Zhang, J.-Q.; Wang, G.-X. Porous Mo_2C nanorods as an efficient catalyst for the hydrogen evolution reaction. *J. Phys. Chem. Solids* **2019**, *132*, 230−235.
(35) Chen, F.; Wang, S.; He, X.-D.; Liao, J.-Y.; Hu, Q.; Dong, J.-M.; Chen, C.-H. Hollow sphere structured V_2O_3@C as an anode material for high capacity potassium-ion batteries. *J. Mater. Chem. A* **2020**, *8*, 13261−13266.
(36) Cheng, X.; Wang, J.-W.; Xiong, W.; Wang, T.; et al. Greatly enhanced electrocatalytic N_2 reduction over V_2O_3/C by P doping. *ChemNanoMat* **2020**, *6*, 1315−1319.
(37) Wu, M.-X.; Lin, X.; Wang, Y.-D.; Wang, L.; Guo, W.; Qi, D.-D.; Peng, X.-J.; Hagfeldt, A.; Gratzel, M.; Ma, T.-L. Economical Pt-free catalysts for counter electrodes of dye sensitized solar cells. *J. Am. Chem. Soc.* **2012**, *134*, 3419−3428.
(38) Vijayakumar, P.; Senthilpandian, M.; Pandikumar, A.; Ramasamy, P. Electrochemical interfacial charge transfer dynamics and photovoltaic performances of nanofibrous vanadium derivatives based platinum free counter electrodes in dye sensitized solar cells. *Mater. Sci. Eng. B* **2017**, *222*, 7−17.
(39) Yue, G.; Lin, J.-Y.; Tai, S.-Y.; Xiao, Y.; Wu, J. A catalytic composite film of MoS_2/graphene flake as a counter electrode for Pt-free dye-sensitized solar cells. *Electrochim. Acta* **2012**, *85*, 162−168.
(40) Guo, H.-Y.; Han, Q.-J.; Gao, C.-J.; Zheng, H.-K.; Zhu, Y.-Q.; Wu, M.-X. A general approach towards carbon supported metal carbide composites for cobalt redox couple based dye-sensitized solar cells as counter electrodes. *J. Power Sources* **2016**, *332*, 399−405.
(41) Ma, J.; Shen, W.; Yu, F. Graphene-enhanced three-dimensional structures of MoS_2 nanosheets as a counter electrode for Pt-free efficient dye-sensitized solar cells. *J. Power Sources* **2017**, *351*, 58−66.
(42) Wu, K.-Z.; Liu, Z.-J.; Wu, M.-M.; Ruan, B.; Wu, R.-T.; Zhou, H.-W.; Wu, M.-X. Economically viable V_2O_3@activated carbon composite materials as counter electrodes for dye sensitized solar cells by single step reduction. *J. Electroanal. Chem.* **2019**, *835*, 150−155.
(43) Gnanasekar, S.; Kollu, P.; Jeong, S.; Grace, A. Pt-free, low-cost and efficient counter electrode with carbon wrapped VO_2(M) nanofiber for dye-sensitized solar cells. *Sci. Rep.* **2019**, *9*, No. 5177.
(44) Hao, L.-T.; Zhang, B.-G.; Cheng, M.; Feng, C.-P. Effects of various organic carbon sources on simultaneous V(V) reduction and bioelectricity generation in single chamber microbial fuel cells. *Bioresour. Technol.* **2016**, *201*, 105−110.
(45) Dilokekunakul, W.; Teerachawanwong, P.; Klomkliang, N.; Supasitmongkol, S.; Chaemchuen, S. Effects of nitrogen and oxygen functional groups and pore width of activated carbon on carbon dioxide capture: temperature dependence. *Chem. Eng. J.* **2020**, *389*, No. 124413.
(46) Sgobba, E.; Stumpf, A.; Vortmann, M.; Jagmann, N.; Krehenbrink, M.; Dirkshofmeister, M.; Moerschbacher, B.; Philipp, B.; Wendisch, V. Synthetic escherichia coli-corynebacterium glutamicum consortia for L-lysine production from starch and sucrose. *Bioresour. Technol.* **2018**, *260*, 302−310.
(47) Li, Y.-Z.; Jiang, Y.-P.; Wang, T.-J.; Zhang, C.; Wang, H.-F. Performance of fluoride electrosorption using micropore-dominant activated carbon as an electrode. *Sep. Purif. Technol.* **2017**, *172*, 415−421.
(48) Geng, X.; Li, L.; Li, F. Carbon nanotubes/activated carbon hybrid with ultrahigh surface area for electrochemical capacitors. *Electrochim. Acta* **2015**, *168*, 25−31.
(49) Qie, L.; Chen, W.-M.; Wang, Z.-H.; Shao, Q.-G.; Li, X.; Yuan, L.-X.; et al. Nitrogen-doped porous carbon nanofiber webs as anodes for lithium ion batteries with a super high capacity and rate capability. *Adv. Mater.* **2012**, *24*, 2047−2050.
(50) Xu, H.-F.; Zhu, G.; Jin, Z. Electron migration optimization through nanostructural control of hierarchical Fe_3O_4 based counter electrodes for high-performance dye-sensitized solar cells. *J. Electroanal. Chem.* **2020**, *869*, No. 114214.
(51) Qi, X.; Meng, Z.-K.; Pan, C.-X. Structure and electrical conductivity of amorphous solid-core carbon nanofibers produced in flames. *Carbon* **2015**, *85*, 447.
(52) Park, H.; Chung, J.; Lim, B.-i.; Jung, C. Design of highly capacitive and durable supercapacitors using activated carbons with different pore structures: petroleum coke and oil palm. *J. Ind. Eng. Chem.* **2019**, *80*, 301−310.
(53) Abioye, A. M.; Noorden, Z. A.; Ani, F. N. Synthesis and characterizations of electroless oil palm shell based-activated carbon/nickel oxide nanocomposite electrodes for supercapacitor applications. *Electrochim. Acta* **2017**, *225*, 493−502.
(54) Vijaya, S.; Landi, G.; Wu, J. J.; Anandan, S. Ni_3S_4/CoS_2 mixed-phase nanocomposite as counter electrode for Pt-free dye-sensitized solar cells. *J. Power Sources* **2020**, *478*, No. 229068.
(55) Lin, X.; Wu, M.-X.; Wang, Y.-D.; Hagfeldt, A.; Ma, T.-L. Novel counter electrode of niobium oxides supersede Pt for dye-sensitized solar cells. *Chem. Commun.* **2011**, *47*, 11489−11491.
(56) Cheng, F.-Y.; Zhang, T.-R.; Zhang, Y.; Du, J.; Han, X.-P.; Chen, J. Enhancing electrocatalytic oxygen reduction on MnO_2 with vacancies. *Angew. Chem., Int. Ed.* **2013**, *52*, 2474−2477.
(57) Ma, J.; Song, Q.-F.; Zhang, F.-B.; Wu, M.-X. Improvement on the catalytic activity of the flexible PEDOT counter electrode in dye-sensitized solar cells. *Mater. Res. Bull.* **2018**, *100*, 213−219.
(58) Makhlouf, M.; Abdulkarim, S.; Adam, S.; Qiao, Q.-Q. Unraveling urea pre-treatment correlated to activate $Er_2(WO_4)_3$ as an efficient and stable counter electrode for dye-sensitized solar cells. *Electrochim. Acta* **2020**, *333*, No. 135540.
(59) Wu, K.-Z.; Sun, X.-L.; Duan, C.-Y.; Gao, J.; Wu, M.-X. Vanadium oxides (V_2O_5) prepared with different methods as counter electrodes in dye-sensitized solar cells (DSCs). *Appl. Phys. A* **2016**, *122*, No. 787.
(60) Sun, L.; Tian, C.-G.; Li, M.-T.; Meng, X.-Y.; Wang, L.; Wang, R.-H.; Yin, J.; Fu, H.-G. From coconut shell to porous grapheme-like nanosheets for high-power supercapacitors. *J. Mater. Chem. A* **2013**, *1*, 6462.
(61) Li, Z.-X.; Ma, Z.-Y.; Zhang, X.; Du, Q.-Z.; Fu, Y.-H.; Shuang, L.; Yang, K.; Li, L.; Lai, W.-D.; Zhang, W.-M. In-situ growth $NiMoS_3$ nanoparticles onto electrospinning synthesis carbon nanofibers as a low cost platinum-free counter electrode for dye-sensitized solar cells. *J. Alloys Compd.* **2021**, *850*, No. 156807.
(62) Sarkar, A.; Bera, S.; Chakraborty, A. K. $CoNi_2S_4$-reduced graphene oxide nanohybrid: An excellent counter electrode for Pt-free DSSC. *Sol. Energy* **2020**, *208*, 139−149.
(63) Gnanasekar, S.; Sonar, P.; Jain, S. M.; Jeong, S. K.; Grace, A. N. Performance evaluation of a low-cost, novel vanadium nitride xerogel

https://doi.org/10.1021/acsomega.0c05880
ACS Omega 2021, 6, 11183−11191

(VNXG) as a platinum-free electrocatalyst for dye-sensitized solar cells. *RSC Adv.* **2020**, *10*, 41177.
(64) Jana, S. K.; Majumder, T.; Banerjee, S. Enhanced photoelectrochemical property of gold nanoparticle sensitized TiO_2 nanotube: A crucial investigation at electrode−electrolyte interface. *J. Electroanal. Chem.* **2014**, *727*, 99−103.
(65) Akın, S.; Erol, E.; Sonmezoglu, S. Enhancing the electron transfer and band potential tuning with long-term stability of ZnO based dye-sensitized solar cells by gallium and tellurium as dual-doping. *Electrochim. Acta* **2017**, *225*, 243−254.

https://doi.org/10.1021/acsomega.0c05880
ACS Omega 2021, 6, 11183−11191